Bright synchrotron radiation from nano-forest targets

Zs. Lécz[1,a)] and A. Andreev[1,2]
[1]*ELI-ALPS, ELI-HU Nonprofit Ltd. Dugonics square 13., 6720 Szeged, Hungary*
[2]*Max-Born Institute, Berlin, Germany*

(Received 21 November 2016; accepted 1 March 2017; published online 17 March 2017)

This paper proposes an intense x-ray source based on the interactions of intense laser pulses with nanowire targets. The presented electron dynamics and energy scalings have been studied by three dimensional particle-in-cell simulations. The resonance of the electronic betatron oscillations with the incident laser field results in extremely high energy electrons. The scaling of radiation intensity is predicted to be $\sim I_L^{5/2}$, where I_L is the laser intensity, using optimal parameters. In this case, the number of photons emitted, via synchrotron radiation, with energies above the keV level with 0.1 rad angular spread is greater than 10^8/fs for intensities $I_L > 10^{20}$ W/cm^2. This scaling law suggests that the photon flux production using nanowires of suitable lengths is much greater than in a underdense plasma. *Published by AIP Publishing.* [http://dx.doi.org/10.1063/1.4978573]

I. INTRODUCTION

Intense ultra-short laser pulses interacting with nanostructured solid surfaces have been considered for enhanced hot electron generation[1] and consequently ion acceleration.[2] More recently, such targets have been proposed to generate ultra-high energy density matter via volumetric heating[3] or Z-pinching of nanorods.[4] The efficient transfer and acceleration of electrons deep into the overdense plasma are possible if the prohibiting magnetic instabilities are eliminated and if the interaction region is much longer than the plasma skin depth. Weibel-type instabilities, due to the high fast electron current induced by the ponderomotive pressure, stop the majority of the electrons before they reach the rear side of the target. This effect can be suppressed if the target surface is expanded before the arrival of the main pulse and if the self-generated fields guide the electrons in the underdense region of the preplasma.[5] The strength of guiding fields is higher if the plasma density is higher, and thus it can be realized with solid density targets if the target surface is micro-engineered. The first proof-of-principle experiment[6] has shown recently that the fast electron energy distribution can be controlled by using nano-forest targets made of nanorods (or nanowires), with a diameter of ~100 nm, grown on a metal surface and separated by several microns.

The efficient heating and transfer of fast electrons with small divergence are crucial in many laser-plasma based ion acceleration mechanisms and even in the fast ignition schemes for controlled fusion reactions.[7,8] The nanoforest target provides multiple guiding channels next to each other with a transversal extent defined by the laser spot size, while in gas targets, the enhancement of electron acceleration occurs in a single ion channel.[9] Due to the cylindrical symmetric target components, the resulting electron motion is rotational rather than planar, and thus three dimensional (3D) modeling is necessary to correctly describe the electron dynamics. Here, we present the results of 3D Particle-in-Cell (PIC) simulations, giving insights into the details of such complex laser-plasma interactions.

This paper also investigates the secondary radiation emitted by the ultra-fast electrons efficiently accelerated in the self-generated fields. Under the right conditions, the fastest electrons undergo betatron resonance during motion around the nanowires and gain high energy. The highly relativistic longitudinal velocity and relatively slow transverse oscillation are ideal for high frequency synchrotron emission in the forward direction. Such high harmonic generation has been investigated using microhole targets with circularly polarized (CP) laser pulses,[10] where coherent radiation was observed in the form of attospirals. In the present paper, nano-bunching of electrons does not occur because the resonant electrons are randomly captured by the guiding fields. However, the efficiency of energy conversion from the incident pulse to the high frequency waves can be higher than in other forward emissions of coherent synchrotron radiation (SR).[11–13]

II. NUMERICAL METHODS

A. Particle in cell simulation

The dependency of the maximum electron energy as a function of target parameters (distance between nano-wires, D_{sp}, and diameter of nanowire, d_w) was studied using 2D particle-in-cell (PIC) simulations and is presented in the supplementary material. It was found necessary to study the interaction in 3D with an identical simulation setup with the interaction length or the length of nanowires of $L_w = 30\,\mu$m and a plasma density of $n_0 = 40 n_{cr}$, where $n_{cr} = \omega_0^2 m_e \epsilon_0 / e^2$ is the critical density. This electron density corresponds to the CH material (carbohydrate) or frozen hydrogen target, but carbon or silicon targets, expanded due to laser prepulse, could also be considered. The FWHM pulse duration is $t_L = 30$ fs at an intensity of $I_L = 6.3 \times 10^{19}$ W/cm^2, which is increased to higher values in further simulations, and the wavelength is $\lambda_l = 800$ nm. Transversally periodic boundaries and uniform laser intensity are used. The grid size is

a)Electronic mail: zsolt.lecz@eli-alps.hu

10 nm in each directions, which is smaller than the laser skin depth, $l_s = c/\omega_p \approx 20$ nm, where $\omega_p = (n_0 e^2/(m_e \epsilon_0))^{1/2}$ is the plasma frequency. 20 macroparticles (ions and electrons) are loaded into each grid cell occupied by the overdense plasma. A distance of $D_{sp} = 1\,\mu$m was chosen for the wire spacing distance, and the effect of the wire thickness was investigated.

Fig. 1 shows an example with a laser pulse polarized in the y direction. Two separate electron populations are clearly visible with the slow electrons flowing in the wire contributing to the return current and fast electrons propagating between the wires where they are subsequently accelerated by the laser pulse. The quasi-static magnetic field generated around the wires dominates the first few laser cycles and prohibits the evolution of magnetic filaments or instability in the cloud of fast electrons, thus allowing the transfer of energy over longer distances. The bottom picture in Fig. 1 (at later time) shows that the return current is very low due to the complete removal of electrons from the wire. In this region, i.e., in the second half of the laser pulse, the electrostatic field is stronger and the electron motion is different.

The ions are immobile in the simulations because the time scale of Coulomb-explosion of the wires is on the order of 10 fs; therefore, the effect of wire expansion is significant only behind the peak of the laser envelope, where ultrafast electrons are not generated.[1] The initial contraction of pinching cold electron delays the expansion of the wires.[4] In 2D simulations, no significant expansion was observed during the traverse time of the laser pulse,[1,14] but longer laser pulses would need to include ion motion.

B. Synchrotron spectrum calculations

The energy transfer from the electrons to the x-ray is not modeled in the PIC code, and thus the results presented here are based on the synchrotron theory of a single electron.[15] Ten thousands macro-electrons are tracked in the simulation in order for good statistics on the emitted radiation. The

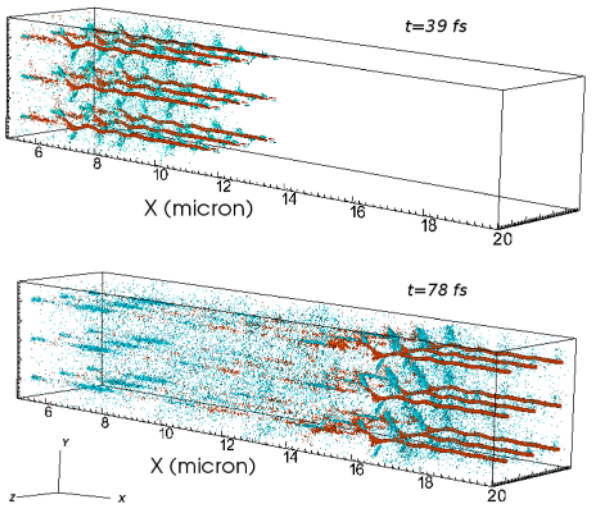

FIG. 1. Electrons contributing to the return current (red, $j_x = 7 \times 10^{17}$ A/m^2) and forward propagating fast electrons (light blue, $j_x = -5 \times 10^{16}$ A/m^2) at two time instances from a 3D simulation with $d_w = 90$ nm. The transversal size of the simulation domain is $3 \times 3\,\mu$m^2.

electron coordinates and momentum are recorded at every time step. The acceleration components can be calculated from the electron trajectory coordinates and momentum, and thus the emitted radiation can be estimated numerically. The expected energy spectrum can be calculated using the expression given for SR integrated over all angles numerically[15]

$$\frac{dW}{d\omega} = \frac{\sqrt{3}e^2}{4\pi\epsilon_0 c}\gamma\frac{\omega}{\omega_c}\int_{\frac{\omega}{\omega_c}}^{\infty} K_{5/3}(x)dx, \tag{1}$$

where $K_n(x)$ is the modified Bessel function of the second kind and $\omega_c = (3/2)\gamma^2(|dp_\perp|/dt/(m_e c))$ is the critical frequency.[13,16] In this method, the radiation is assumed to be emitted in the direction of the electron velocity vector and thus only the transversal acceleration is taken into account, $|dp_\perp|/dt$, where dt is the time step of the simulation. The emission angle used throughout this paper is defined as $\theta = \arctan(p_\perp/p_x)$. As the emission of high energy photons is the primary focus of this paper, the synchrotron spectrum is calculated only if the electron energy is above a chosen value (or $\gamma > \gamma_b$). In this way, the radiation emitted by N_{tr} tracked macro-electrons is calculated. In order to obtain the total radiated energy, the spectral intensity is multiplied by the ratio N_{all}/N_{tr}, where N_{all} is the number of counted electrons (tracked and non-tracked) with $\gamma > \gamma_b$. A comparison between this sampling method and a Monte Carlo algorithm implemented in other PIC codes is presented in the supplementary material.

III. RESULTS

A. Electron dynamics

The electron guiding and betatron oscillation are possible due to the self-generated radial electric and azimuthal magnetic fields near the nanowires. The magnetic field is more persistent when thicker or denser wires are used as there is no complete extraction of the electrons from the plasma.[4] In the case of long pulses, electrons will also be removed from the thick wires at a later time but before the significant expansion of the wires. Therefore, the interaction will always consist of two parts:[14] initially, the magnetic field, driven by the return current, contributes to the electron guiding, but later, only the charge separation field and laser fields define the motion.

The electrostatic field dominates in thinner wires, and the electron dynamics depend on the ratio of the static electric field and laser field amplitude. If the wire is thinner than the critical thickness, $d_{cr} = a_0(n_{cr}/n_0)\lambda_l/\pi \approx 34$ nm (for our parameters), then all electrons are extracted within one laser wavelength, where $a_0 = eE_L/(m_e\omega_0 c)$ is the normalized laser field amplitude with the laser frequency ω_0. This critical thickness is valid for one laser period, but the interaction and the pulse duration are much longer. Therefore, the complete removal of electrons is also possible for thicker wires for a pulse of suitable length (see Fig. 1). The parameter $n = E_L/E_s$, where E_s is the static electric field, is introduced to characterize the interaction, and this parameter is approximated with the function $n(d_w) = N_L d_{cr}/(d_w)$, for $d_w < N_L d_{cr}$, where N_L is the number of laser cycles and $N_L d_{cr}$ can be

defined as the effective critical thickness. This expression ensures that $E_s \to 0$ if $d_w \to 0$ and $E_s \approx E_L$ if $d_w \to N_L d_{cr}$. This work, presented here, only considers the thin wire regime, i.e., $n \gg 1$.

The 2D simulations show that there is an optimal wire thickness for the S-polarized interaction that results in maximizing the electron energy. This maximum can be attributed to a resonance between the electron betatron oscillation and laser field.[14] However, the crossing of nano-wires makes the 2D simulations unrealistic, but these 2D results (presented in the supplementary material) are, however, applicable for nano-plates, which according to the simulations could allow the control of synchrotron emission by changing the plate thickness or laser polarization.

Fig. 2(a) shows the electron spectra obtained from 3D simulations. These show that the resonant conditions are different from the planar geometry simulation because the maximum cut-off energy is obtained for $d_w = 60$ nm, while the 2D maximum γ-factor was measured for a much thinner wire. The energy conversion efficiency is calculated as $\eta = W_e/W_L$, where W_e is the total energy of electrons at the end of the interaction and W_L is the pulse energy. The total energy conversion is defined as $\eta_{tot} = (W_e + W_{rad})/W_L$, where W_{rad} is the energy of short wavelength radiation, which cannot be represented on the grid of this PIC simulation. The SR energy is calculated with the presented post-processor algorithm which relies on the trajectory of electrons. The energy emitted by an electron during one time step is much smaller than its kinetic energy, but at ultra-relativistic intensities, W_{rad} can be comparable with W_e, and thus radiation dumping has to be included.

Fig. 2(b) shows the trajectories of a few electrons plotted for thin (blue) and intermediate thickness (red) wires. In Fig. 2(c), it can be seen that the momentum of slower electrons oscillates for a relatively long time and does not increase at the same rate as in the thicker wire scenario. This oscillation happens in the direction of laser polarization (y, Fig. 2(b)). It seems that in the case of $d_w = 60$ nm, the electrons reach the resonant condition earlier and are accelerated between the nanowires in the laser field. Initially, the electrons have small γ and oscillate freely in the laser field without gaining energy. The laser field, as well as the static field, increases during the interaction, due to the Gaussian pulse envelope, and after a few laser cycles, it reaches the value needed for resonance. This process takes longer for thinner wires, which can be seen from the delay in the electron acceleration for $d_w = 30$ nm in Fig. 2(c).

The physical process behind the synchrotron emission has been observed and explained in earlier works.[13,14] Resonance occurs during the spiral motion of electrons around wires when the relativistically corrected ion plasma frequency approaches the laser frequency experienced by the electrons: $\omega_0' = \omega_0(1 - v_x/c)$. In order to understand the role of wire thickness in the motion of electrons, the resonance condition starting from the equation of motion along the laser polarization was derived (the full set of equations is in the supplementary material)

$$\frac{dp_y}{dt} = -E_L + v_x(B_s \sin(\alpha) + B_L) - E_s \sin(\alpha), \tag{2}$$

and using the energy equation

$$\frac{d\gamma}{dt} = -v_y E_L - v_y E_s \sin(\alpha) - v_z E_s \cos(\alpha), \tag{3}$$

where $E_L = E_{L0} \sin(t - x/v_{ph})$ is the laser electric field, E_s is the static electric field, and $B_s = mE_s$ is the corresponding magnetic field induced by the return current. Here, $\alpha = \arctan(y/z)$ is the azimuthal angle, $r = \sqrt{y^2 + z^2}$ is the radius measured from the center of the nanowire. The following normalizations are used: $p \to p/m_e c$, $v \to v/c$, $t \to \omega_0 t$, $x \to x\omega_0/c$, $E \to eE/(m_e \omega_0 c)$ and $B \to eB/(m_e \omega_0)$.

In order to obtain analytical expressions, the analysis is restricted to very weak static fields ($n > 1, m \approx 0$), when the electron oscillation in the z direction is negligible and a linear function for the spatial distribution of the static fields is used: $E_s = (E_{L0}/n)(1 - |y|/R_{sp})$, where R_{sp} is the half distance between nanowires. The equation of a driven oscillator is obtained by rewriting Eq. (4)

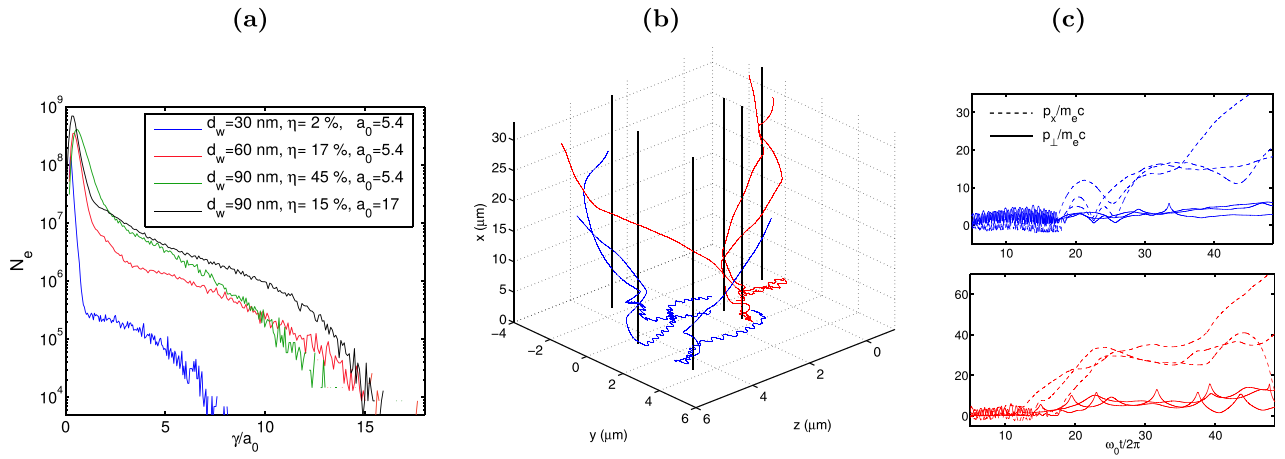

FIG. 2. (a) Energy spectrum of electrons from the 3D simulations at the end of the interaction ($t = 160$ fs). (b) Electron trajectories from simulations indicated with blue ($d_w = 30$ nm) and red ($d_w = 60$ nm) colors in (a). The vertical black lines illustrate several nanowires. The corresponding time history of momentum components is shown in (c).

$$\frac{d^2y}{dt^2} + y\frac{K_E}{R_{sp}} = -K_E n\Omega \sin(\Omega t) - K_E, \tag{4}$$

where $\Omega = 1 - v_x/v_{ph}$, $K_E = E_{L0}/(n\gamma)$, and we used the approximation $\sin(\alpha) \approx 1$. Another assumption made is that the small size of the oscillation amplitude $dy/dt \ll 1$, and thus $(dy/dt)^2 \approx 0$. Now, we can seek for the solution of Eq. (4) in the form $y = A\cos(\Omega t - \phi)$. After some algebra, one finds the expression for amplitude

$$A = \frac{K_E\sqrt{1+n^2\Omega^2}}{\Omega^2 - K_E/R_{sp}} \tag{5}$$

and for the phase $\tan(\phi) = n\Omega$. The resonant frequency is obtained when the denominator of the amplitude is zero, which yields $\Omega_r = \sqrt{E_{L0}/(n\gamma R_{sp})}$, the eigenfrequency of Eq. (4). Substituting the expression of n into the equation $\Omega_r = \omega_0'$, one finds the resonant wire thickness

$$d_w^{res} = \frac{n_{cr}}{n_0} G \frac{N_L D_{sp}}{2}, \tag{6}$$

where $G = (\gamma - \sqrt{\gamma^2 - (p_\perp/m_e c)^2} - 1)^2/\gamma$ with $p_\perp = \sqrt{p_y^2 + p_z^2}$ being the transversal component of the electron momentum. The value of G varies from 0 to γ as $p_\perp$ increases. During the initial electron oscillation, it is more probable that $p_\perp > p_x$, which means a larger G, and thus, in the case of thicker wires, more electrons can satisfy the resonance condition given in Eq. (6). For thin wires, this condition is rarely satisfied, which explains the observed behavior in Fig. 2. The resonant acceleration loses its efficiency (and the model is invalid) when the wire thickness is increased to the point that the laser energy absorption becomes significant ($\eta > 30\%$).

B. Synchrotron radiation

There are features in the radiation, which appear in both the 2D and 3D simulations. The distribution of emitted radiation is shown in Fig. 3. In the case of the bottom pictures of Fig. 3, the synchrotron spectrum is calculated in each time step and integrated to obtain the radiated energy at a given (θ_y, θ_z) angle. The divergence angle is much smaller for the thinner wire, as in 2D, but the radiated energy is also smaller. The laser pulse is polarized in the y direction, and thus, according to the 2D results, the divergence should be larger in this direction. This can be observed in the bottom pictures of Fig. 3, where the shape of intense radiation is elongated along the θ_y angle and narrower in θ_z in both cases. The emitted total energy is on the order of 7.6 μJ for $d_w = 60$ nm. The pulse energy is $W_L = 90$ mJ, resulting in an energy conversion efficiency of $\eta_{lx} \approx 8.5 \times 10^{-5}$ from the laser to the x-ray.

Figure 4(a) shows the spectrum of emitted photons for linear and circular polarization. It can be seen that the number of photons above keV energy is more than 10^9—larger than other laser-solid x-ray sources.[13] The nanowire generated photon flux (N_{ph}/t_L) is comparable to the flux generated

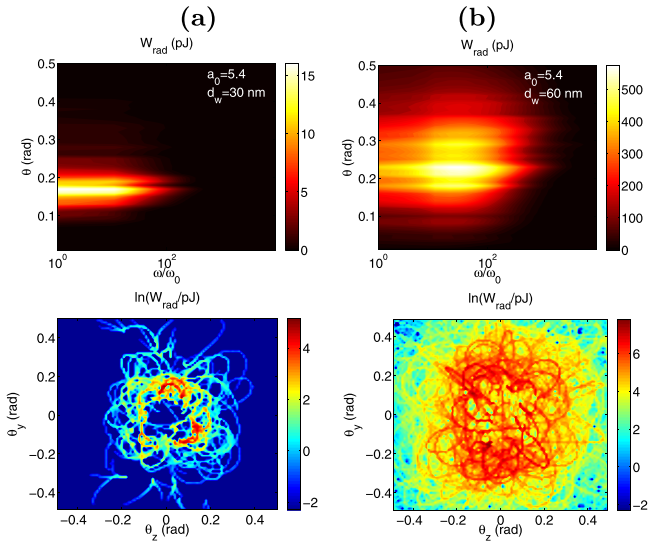

FIG. 3. Spectral-angular intensity distribution of radiation for $D_{sp} = 1\ \mu$m: $d_w = 30$ nm (a) and $d_w = 60$ nm (b). Only electrons with $\gamma > 10$ are included. The corresponding angular distribution of the radiated energy is shown below, where the angles are defined as $\theta_y = \arctan(v_y/v_x)$ and $\theta_z = \arctan(v_z/v_x)$.

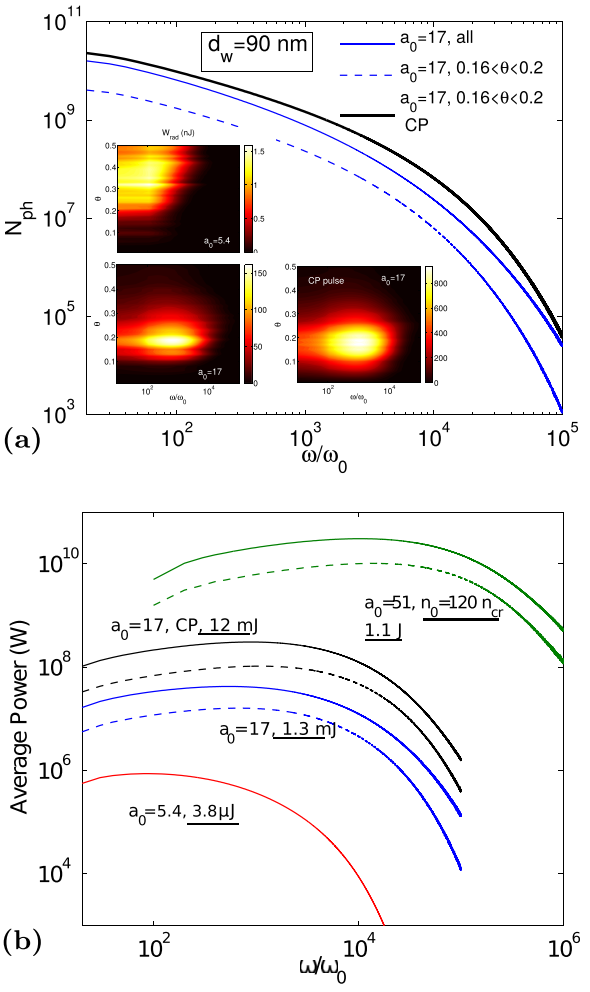

FIG. 4. (a) Spectrum of photons emitted in the case of circular and linear polarization. For comparison, one intensity spectrum for lower laser intensity is also shown in the inset. (b) Comparison of the power spectra and total energy of synchrotron radiation (underlined) for different intensities. The dashed lines show the energy spectra measured between angles 0.16 and 0.2 rad. Here, electrons with $\gamma > 20$ are included.

in the underdense plasma,[16,17] but the laser propagation length is 100 times shorter. A much higher photon flux can be anticipated by considering a much longer interaction length and the efficient guiding of electrons. The distribution of the radiation, shown in the inset of Fig. 4(a), has a larger angular spread in the case of lower intensity because the wire thickness is closer to the effective critical thickness.

The target has cylindrical symmetry, and thus, it can be assumed that with circularly polarized (CP) laser pulses, the electron acceleration should be more efficient, resulting in the production of higher energy photons. Fig. 4(b) shows that a higher maximum photon energy is reached, and the conversion efficiency is increased from $\eta_{lx} = 0.067\%$ to $\eta_{lx} = 0.3\%$ calculated for the cone angle $0.16 < \theta < 0.2$. Although the resonance condition is the same for CP pulses (proven by analytical calculations in the supplementary material), more electrons can be accelerated, and some of them gain higher energy due to the constant ponderomotive force. The shift of the peak of spectral intensity, towards higher photon energies, is proportional to the laser intensity—Fig. 4(b). The observed scaling of the spectral peak can be written as $\omega_{peak} \approx 5a_0^2\omega_0$, which is larger than the theoretical peak:[15] 0.3 $\omega_c \approx 0.5a_0^3\omega_0$ for $a_0 < 10$, where the average gamma-factor of electrons is considered, $\langle\gamma\rangle \approx a_0$.

The electrons to x-ray energy conversion efficiency can be higher in the case of higher laser intensities because the radiative energy loss is proportional to $\omega_c\gamma \sim \gamma^4$.[16] The energy gain of electrons is proportional to the laser field and interaction length, $\gamma \sim \sqrt{I_L}L_w$, and thus $\eta_{ex} \sim I_L^2L_w^4$. The scaling of the radiation intensity can be expressed as $I_{rad} = \eta_{lx}I_L$, where $\eta_{lx} = \eta\eta_{ex}$ and $\eta \approx N_e\gamma m_e c^2/I_L \sim n_0L_wN_Ld_w^2/\sqrt{I_L}$, where $N_e = N_L\lambda_l n_0\pi d_w^2/4$. Using the expression for critical thickness, the absorption efficiency becomes $\eta \sim L_wN_L(d_w/d_{cr})^2a_0n_{cr}^2/n_0$, which is $\eta \sim N_Ld_w^2/a_0$ for constant density and wire length. Finally, the scaling law is obtained

$$I_{rad} \sim n_0I_L^{5/2}N_LL_w^5, \quad \text{if } d_w = \text{constant}. \tag{7}$$

This expression is valid for infinitely large laser spot size and if all radiation is emitted with small radiation divergence. This energy scaling is supported by the energy values indicated in Fig. 4(b), where in the case of $d_w = 90$ nm, the total radiated energy is $10^{2.5} \approx 300$ times larger after increasing I_L 10 times. It follows from Eq. (7) that the radiation intensity scales as $\sim I_L^3 \sim a_0^6$ with the same relative thickness, $n_0 \sim a_0$, which is in agreement with the results presented in Fig. 4(b). This scaling is not valid at ultra-high laser intensities because the radiation reaction effects become important, and the photon emission has to be modeled self-consistently within the PIC code.[18] In the thick wire regime, the volumetric heating dominates, which results in strong thermal x-ray emission,[3] which has much longer wavelength. In our case (thin wires), it was found that the collimated forward SR is stronger than the bremsstrahlung radiation.[14]

The total energy of electrons and radiation is shown in Fig. 5 as a function of wire thickness corresponding to the simulations with $I_L = 6.3 \times 10^{19}$ W/cm^2. As expected, the energy transferred to electrons increases by increasing the wire thickness, but the energy of photons emitted within a small cone angle is the strongest for $d_w = 60$ nm. For $d_w = 90$ nm, the total radiated energy is the same as for $d_w = 60$ nm, but the angular spread is larger. The optimal wire thickness for this laser intensity is $\approx 2d_{cr}$, but it does not manifest a pronounced enhancement of electron acceleration as in 2D.[14] At higher intensities, the optimal thickness scales with $\sqrt{a_0}$ because $\eta \sim d_w^2/a_0$ and the laser-to-electron conversion efficiency has to be $\eta \approx 15\%$–20%. From these considerations and simulation results, an empirical formula for optimal thickness can be defined: $d_w^{opt} \approx 4d_{cr}/\sqrt{a_0} = (4/\pi)\sqrt{a_0}(n_{cr}/n_0)\lambda_l$.

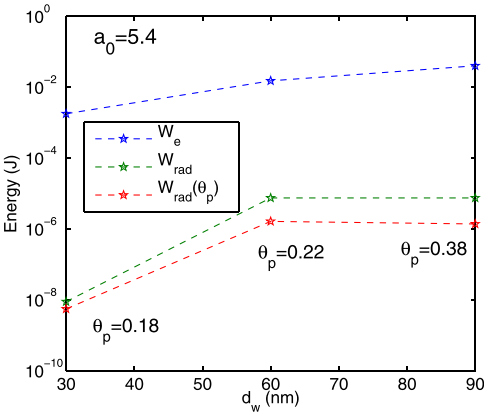

FIG. 5. Different energies measured at the end of the interaction in the simulation. The value of θ_p is the angle at which the radiation intensity is the strongest, and the red lines show the radiation energy measured within 0.05 rad opening angle centered at θ_p. In all cases, the laser pulse energy is 90 mJ.

IV. CONCLUSIONS

The interaction of short, intense laser pulses with parallel nanowires of 10s μm length has been studied. The thin wire regime ($d_w < N_Ld_{cr}$) has been considered where, after a short time, all electrons can be extracted from the target. A part of these electrons undergo betatron oscillation, which may be in resonance with the laser field. Due to the resonant acceleration, high energy electrons are generated, which in turn emit strong synchrotron radiation with characteristics depending on the wire thickness. There is an optimal thickness, defined by the target electron density and laser intensity, which ensures efficient acceleration and relatively small emission cone angle (≈ 0.1 rad). The simulation results and the analytical scaling suggest that the produced photon flux with such a target can be much higher than in the case of the underdense plasma if the wire and laser pulse are long enough.

At moderate intensities, this type of x-ray source could be further optimized and tested with non-parallel wires, giving rise to a more collimated and brighter synchrotron emission. In the case of convergent wires, the electrons could be initially accelerated by resonance until the distance between wires would be so short that the electrons are forced to oscillate around the wires losing more energy to x-ray radiation.

SUPPLEMENTARY MATERIAL

The supplementary material contains complementary information which supports the results presented in this

paper. The first section of this document presents a parameter-scan performed in two dimensional simulations and expresses the difference compared with more realistic 3D simulations. The second section contains a benchmarking of our post-processing method. The third section includes a more extended analysis of the electron dynamics where the equations of motion are solved numerically, giving a qualitative agreement with the self-consistent PIC simulations.

ACKNOWLEDGMENTS

The authors would like to thank the developer team of Tech-X Corporation for the help and support in solving the issues regarding the parallel performance of the simulation code (VSim). The high performance computer cluster was provided by the John Adams Institute (Oxford) supported by the UK STFC for JAI, Grant No. ST/J002011/1. The ELI-ALPS project (GOP-1.1.1.-12/B-2012-0001 and GINOP-2.3.6-15-2015-00001) was supported by the European Union and co-financed by the European Regional Development Fund.

[1]A. A. Andreev and K. Yu. Platonov, Opt. Spectrosc. **117**, 287–303 (2014).
[2]A. Andreev, N. Kumar, K. Platonov, and A. Pukhov, Phys. Plasmas **18**, 103103 (2011).
[3]V. Kaymak, A. Pukhov, V. N. Shlyaptsev, and J. J. Rocca, Phys. Rev. Lett. **117**, 035004 (2016).
[4]C. Bargsten, R. Hollinger, M. G. Capeluto, V. Kaymak, A. Pukhov, S. Wang, A. Rockwood, Y. Wang, D. Keiss, R. Tommasini, R. London, J. Park, M. Busquet, M. Klapisch, V. N. Shlyaptsev, and J. J. Rocca, Sci. Adv. **3**, 1601558 (2017).
[5]A. Pukhov, Z.-M. Sheng, and J. Meyer-ter-Vehn, Phys. Plasmas **6**, 2847 (1999).
[6]S. Jiang, L. L. Ji, H. Audesirk, K. M. George, J. Snyder, A. Krygier, P. Poole, C. Willis, R. Daskalova, E. Chowdhury, N. S. Lewis, D. W. Schumacher, A. Pukhov, R. R. Freeman, and K. U. Akli, Phys. Rev. Lett. **116**, 085002 (2016).
[7]Y. Sentoku, K. Mima, H. Ruhl, Y. Toyama, R. Kodama, and T. E. Cowan, Phys. Plasmas **11**, 3083 (2004).
[8]B. F. Lasinski, A. B. Langdon, S. P. Hatchett, M. H. Key, and M. Tabak, Phys. Plasmas **6**, 2041 (1999).
[9]A. V. Arefiev, V. N. Khudik, and M. Schollmeier, Phys. Plasmas **21**, 033104 (2014).
[10]Zs. Lecz and A. Andreev, Phys. Rev. E **93**, 013207 (2016).
[11]H. George, F. Quéré, C. Thaury, G. Bonnaud, and Ph. Martin, New J. Phys. **11**, 113028 (2009).
[12]B. Dromey, S. Rykovanov, M. Yeung, R. Horlein, D. Jung, D. C. Gautier, T. Dzelzainis, D. Kiefer, S. Palaniyppan, R. Shah, J. Schreiber, H. Ruhl, J. C. Fernandez, C. L. S. Lewis, M. Zepf, and B. M. Hegelich, Nat. Phys. **8**, 804 (2012).
[13]T. P. Yu, A. Pukhov, Z.-M. Sheng, F. Liu, and G. Shvets, Phys. Rev. Lett. **110**, 045001 (2013).
[14]A. Andreev and K. Yu. Platonov, Quantum Electron. **46**, 109–118 (2016).
[15]J. D. Jackson, *Classical Electrodynamics*, 3rd ed. (Hamilton Printing Company, 1999), Chap. 14.6.
[16]S. Kiselev, A. Pukhov, and I. Kostyukov, Phys. Rev. Lett. **93**, 135004 (2004).
[17]I. Kostyukov, S. Kiselev, and A. Pukhov, Phys. Plasmas **10**, 4818 (2003).
[18]C. P. Ridgers, J. G. Kirk, R. Duclous, T. G. Blackburn, C. S. Brady, K. Bennett, T. D. Arber, and A. R. Bell, J. Comput. Phys. **260**, 273–285 (2014).